

# THE EFFECT OF BARYON COOLING ON THE STATISTICS OF GIANT ARCS AND MULTIPLE QUASARS

JOACHIM WAMBSGANSS

Astronomisches Rechen-Institut, Zentrum für Astronomie der Universität Heidelberg, Mönchhofstrasse 12-14,  
 69120 Heidelberg, Germany; jkw@uni-hd.de

AND

JEREMIAH P. OSTRICKER AND PAUL BODE

Department of Astrophysical Sciences, Princeton University, Princeton, NJ 08544;  
 jpo@astro.princeton.edu, bode@astro.princeton.edu

Received 2007 July 10; accepted 2007 December 3

## ABSTRACT

The statistics of giant arcs and large-separation lensed quasars provide powerful constraints for the parameters of the underlying cosmological model. So far, most investigations have been carried out using pure dark matter simulations. Here we present a recipe for including the effects of baryon cooling (i.e., large galaxy formation) in dark matter  $N$ -body simulations that is consistent with observations of massive galaxies. Then we quantitatively compare lensing with and without applying this baryon correction to the pure dark matter case. Including the baryon correction significantly increases the frequency of giant arcs and lensed quasars, particularly on scales of  $10''$  and smaller: the overall frequency of multiple images with splittings larger than  $3''$  increases by about 25% for source redshifts between  $z_s = 1.5$  and 7.5. The baryon rearrangement also slightly increases the fraction of quadruple images over doubles.

*Subject headings:* galaxies: clusters: general — gravitational lensing — quasars: general

*Online material:* color figures

## 1. INTRODUCTION

It has been realized for some time that the abundance of clusters of galaxies can provide very stringent constraints on cosmological models (e.g., Henry & Arnaud 1991; Oukbir & Blanchard 1992; White et al. 1993; Bahcall & Cen 1993; Eke et al. 1996; Viana & Liddle 1996; Bahcall & Bode 2003 and references therein). The reason for this is that since only 5%–10% of the stellar mass is in rich clusters, the exact fraction of which is fixed by the definition of “rich,” they represent relatively rare fluctuations of approximately  $2\sigma$ . Consequently, as they lie on the tail of the density distribution, relatively small changes in the mean amplitude of the cosmic perturbation spectrum can produce large changes in the expected numbers of rich clusters. In fact, gravitational lensing by clusters, which depends on the most dense fraction of these systems, provides an especially sensitive measure of the cosmological parameters (Turner 1990; Wambsganss et al. 1995; Bartelmann et al. 1998; Li & Ostriker 2002, 2003; Li et al. 2007). At the present time there is significant uncertainty in the normalization of the fluctuation power spectrum. For example, Spergel et al. (2007) give an estimate based on *Wilkinson Microwave Anisotropy Probe* (*WMAP*) 3 year and Sloan Digital Sky Survey (SDSS) data that is significantly lower than the *WMAP* 1 year data, but Evrard et al. (2008) argue that the cluster X-ray data indicate a higher normalization cosmology. It is hoped that efforts such as the present paper, based on ray tracing through specific cosmological models, can help resolve this controversy.

The frequency of giant arcs and large-separation quasar lenses has received increasing interest in the last few years as a powerful tool for constraining cosmological parameters. The recent discovery of a few widely separated quasar lenses ( $\Delta\theta \geq 10''$ ) from the Sloan Digital Sky Survey (Inada et al. 2003, 2005, 2006; Oguri et al. 2004; Sharon et al. 2005) has also spurred such studies. Almost all theoretical studies using  $N$ -body simulations are constrained on dark matter only (Bartelmann et al. 1998;

Wambsganss et al. 1995, 1997, 1998; Meneghetti et al. 2003; Wambsganss et al. 2004; Dalal et al. 2004; Oguri & Keeton 2004; Ho & White 2005; Horesh et al. 2005; Li et al. 2005, 2007; Hennawi et al. 2007a, 2007b; Hilbert et al. 2007). In such studies it is usually assumed that the baryonic matter essentially follows the dark matter (DM) particles. This may be true in general on large scales, but it certainly is not a very good assumption in the central parts of galaxy clusters or for very massive isolated galaxies, which are precisely the essential matter concentrations for the production of giant arcs and wide quasar lenses. The baryonic component is also known to dominate in the central regions of elliptical galaxies.

Recent studies have begun investigating the influence of baryons on DM clustering. Puchwein et al. (2005) looked into the effect of gas physics on strong lensing by individual galaxy clusters. They found that cooling and star formation can increase the strong-lensing efficiency considerably. Jing et al. (2006) studied the influence of baryons on the clustering of matter and weak-lensing surveys, and they found that the clustering of total matter is suppressed by about 1% on large scales of  $1\ h\ \text{Mpc}^{-1} \lesssim k \lesssim 10\ h\ \text{Mpc}^{-1}$ , whereas it is boosted between 2% and 10% on small scales of  $k \approx 20\ h\ \text{Mpc}^{-1}$ . They conclude that this should be measurable with future weak-lensing surveys (Jing et al. 2006). Lin et al. (2006) looked into the influence of baryons on the mass distribution of dark matter halos and found an increase of the concentration parameters by 3%–10% as compared to pure  $N$ -body simulations. Rozo et al. (2006) studied the effect of baryonic cooling on giant arc abundances for individual clusters; they found that the arc abundances can be increased by factors of a few.

In this study we quantitatively investigate the effect of baryon cooling on the statistics of arcs and widely separated multiple quasars. We first motivate and describe a simple recipe for redistributing part of the matter in the centers of halos to approximate the effects of cooling and star formation, and then we present some tests of this method. Subsequently we summarize our use of the

ray-shooting method. Then we describe the quantitative results of our baryon redistribution recipe by directly comparing pseudo-three-dimensional ray-shooting simulations with and without this baryon cooling, and finally we discuss this effect with respect to the observational situation.

## 2. METHODS

### 2.1. Baryon Rearrangement

In order to approximate the effects of galaxy formation in our ray-shooting simulations, we locate halos in all lens planes and identify the amount of mass that is likely to have cooled into stars. This mass will be rearranged such that the inner part of the total profile is isothermal. Such an approach is supported by observations, e.g., those of Peng et al. (2004) and Gavazzi et al. (2007), who found from both kinematical and lensing data that early-type galaxies are consistent with an isothermal profile out to  $\geq 300 h^{-1}$  kpc. In this section we describe in detail how this rearrangement is performed. The goal is to keep the method as simple and flexible as possible. The approach that we adopt is admittedly very rough, and so, as in all semianalytical modeling, we constrain the free parameters to respect observational data. The requirements the model must fulfill are as follows. (1) The fraction of the baryonic component that is rearranged into stellar systems is consistent with the stellar mass fraction of the universe (cf. Figs. 2 and 3). (2) The cosmic buildup of mass in stellar systems parallels what is known from observations (Fig. 3). (3) Individual mass profiles within the baryonically dominated systems are consistent with kinematic and gravitational lensing data (Fig. 4). (4) The distribution of systems as a function of stellar mass and circular velocity approximates observational data (Figs. 2 and 4).

Suppose we have projected the mass in some volume onto a plane for the purpose of ray tracing (as described below in § 2.2). Let us denote the surface density of a given pixel as  $\sigma$  and the pixel size as  $l$ , so that the mass in each pixel is  $\sigma l^2$ . For a given two-dimensional plane, each pixel is examined in turn to see if it has a higher surface density than any other pixel within a radius of roughly the size of the smallest objects resolved in the simulation,  $R_b = 30 h^{-1}$  kpc (physical). If so, this pixel is taken to be the center of a halo. Many of the pixels initially selected in this manner will be spurious peaks due to projection effects, but these are weeded out in subsequent steps; e.g., by ignoring the redistribution effect for cases with  $V_{\text{circ}} < 125 \text{ km s}^{-1}$ . Around each prospective halo in turn, the background surface density  $\sigma_{\text{bg}}$  is set to the mean surface density between  $R_c$  and  $R_c + (R_b/2)$ , for a given cooling radius  $R_c$  (to be determined below). The mass of the halo is defined as

$$M_h = \int W(R/R_c) [\sigma(R) - \sigma_{\text{bg}}] dA, \quad (1)$$

where we integrate from the halo center out to  $R_c$ ; here we will use the window function  $W(x) = (1 - x^2)^2$ . With the mass-weighted radius of the halo given by

$$R_h = M_h^{-1} \int R W(R/R_c) [\sigma(R) - \sigma_{\text{bg}}] dA, \quad (2)$$

the halo temperature is defined as

$$T_h = \frac{G m_p M_h}{k R_h}, \quad (3)$$

where  $G$  and  $k$  are the Newton and Boltzmann constants, respectively, and  $m_p$  is the proton mass.

We wish to find a cooling radius  $R_c$  such that half of the baryons contained within this radius will have formed stars. For ionized gas in a galaxy cluster, the cooling time from bremsstrahlung radiation is given by  $t_{\text{br}} = 9 \times 10^7 T_8^{1/2} n_e^{-1} \text{ yr}$  (cf. Cox 2000, p. 625); here  $n_e$  is the electron density per  $\text{cm}^3$ , which we will take to be  $n_e = 3M_h/(4\pi R_h^3 m_p)$ . Let  $T_0$  be the temperature at which the cooling time equals the age of the universe at the redshift under consideration,  $t_{\text{Hub}}$ :

$$T_0 = n_e^2 \left( \frac{t_{\text{Hub}}}{9 \times 10^7 \text{ yr}} \right)^2 10^8 \text{ K}. \quad (4)$$

To set  $R_c$ , we start with a small estimate for the cooling radius and increase it until

$$e^{-T_h/\eta T_0} = f_*, \quad (5)$$

with the cooled fraction set to  $f_* = \frac{1}{2}$ , is satisfied. A number of oversimplifications have gone into the calculation of  $T_h$  and  $T_0$ , so the variable  $\eta$  is introduced to account for these approximations. This parameter can be adjusted to give more or less stellar mass; we find that a value of  $\eta = \frac{1}{3}$  gives a reasonable amount of stellar mass, consistent with observational constraints. Problems will arise with this algorithm if the aperture  $R_c$  increases to the point where it begins to include neighboring structures, as can happen in the case of a galaxy-sized halo inside a group or cluster. Thus, if during this process it happens that  $R_h/R_c > \frac{1}{3}$ , we stop increasing  $R_c$  and leave the value of  $f_*$  to be larger than  $\frac{1}{2}$ .

Mass representing the cooled baryonic component is then removed from inside  $R_c$ , which reduces the surface density to a temporary value of

$$\sigma_i(R) = \sigma(R) - \frac{\Omega_b}{\Omega_m} f_* W(R/R_c) [\sigma(R) - \sigma_{\text{bg}}], \quad (6)$$

with the caveat that any pixels that are denser than the central pixel are left unchanged. This removed mass is then added back in, using an isothermal profile  $A/R$  within a smaller radius  $R_A$ . With the isothermal component added back in, the final surface density is

$$\sigma_f(R) = \sigma_i(R) + A W(R/R_A)/R. \quad (7)$$

For a given value of  $R_A$  (set below), the value of the constant  $A$  is set by conservation of mass: i.e., the mass put back in,  $M_{\text{stellar}}$ , must of course equal that taken out originally. Figure 1 illustrates how our method of baryon redistribution affects the velocity profile of a halo and its projected surface mass density. In the top panel, the four lines in this example halo show the initial circular velocity from the pure  $N$ -body simulation (*solid line*), the circular velocity after mass removal, as given by equation (6) (*dotted line*), the velocity curve of the isothermal component to be added back in, according to equation (7) (*dot-dashed line*), and the final circular velocity profile after the redistribution is complete (*dashed line*). In the bottom panel, the circularly averaged surface mass density profiles of this same cluster are shown; the four line types are the same as in the top panel. This example corresponds to a brightest cluster galaxy residing at the center of the cluster dark matter halo.

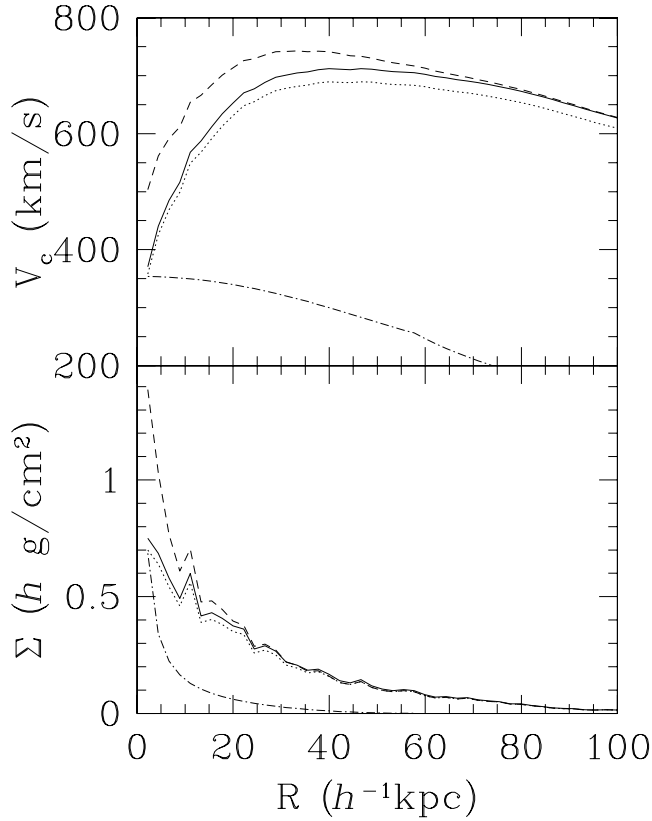


FIG. 1.—*Top*: Circular velocity profile of an example halo, demonstrating the effect of redistribution. The solid line represents the initial circular velocity, the dotted line represents the circular velocity after mass removal (cf. eq. [6]), the dot-dashed line represents the velocity of the isothermal component (cf. eq. [7]), and the dashed line shows the final circular velocity profile. *Bottom*: Surface mass density profiles for the same halo (circularly averaged). The line types have the same meanings as in the top panel.

Figure 2 shows the “stellar mass function” (that is, the distribution of  $M_{\text{stellar}}$ ) in halos identified by our algorithm at the redshifts  $z = 0.05, 0.55$ , and  $1.05$ . The distribution of stellar masses is similar at all three redshifts. The lower dotted line shows the results from taking the luminosity function of SDSS galaxies (Blanton et al. 2003) and assuming a constant value of  $M_{\text{star}}/L = 4.4$  (see Gavazzi et al. 2007); the upper dotted line instead assumes a value of  $M_{\text{star}}/L \propto L^{0.25}$  (Vale & Ostriker 2006).

As a further test, summing the total mass rearranged at a given redshift yields an estimate of the stellar mass in large spheroidal galaxies. The data points in Figure 3 show the density of this component (as a fraction of the critical density) versus redshift. The error bars give the error on the mean value of the 486 planes used; this error becomes larger at low redshift primarily because the physical size of the planes within the “beam” is smaller. The total fraction of mass that is rearranged rises slowly from  $\Omega_* = 0.7 \times 10^{-3}$  at  $z = 1$  to  $\Omega_* = 1.0 \times 10^{-3}$  at  $z = 0.29$ , remaining at this value for lower redshifts. Also shown are empirically based estimates (compiled in Nagamine et al. 2006) for the total mass in elliptical galaxies. The solid line shows the total mass in elliptical (“spheroidal”) components. The dotted line indicates an estimate of the mass limited to systems with  $V_c > 215 \text{ km s}^{-1}$ , which would produce splitting angles of  $>3''$ . These lines bracket our points, indicating that we are not overproducing galaxies, but are including those likely to produce significant lensing.

From these tests we conclude that our choice of  $\eta$ , which determines the mass rearranged in a given halo, is reasonable. The stel-

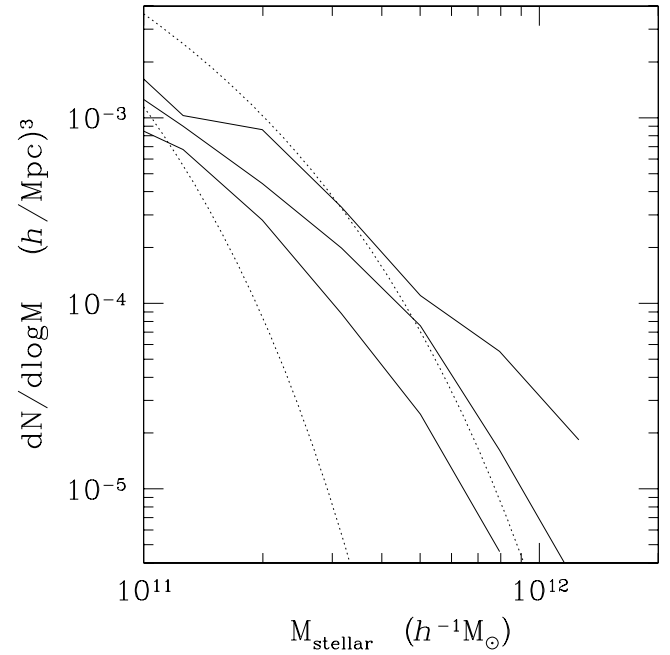


FIG. 2.—Stellar mass functions as determined with the recipe described in the text, at redshifts  $z = 0.05, 0.55$ , and  $1.05$  (solid lines, top to bottom). The lower dotted line shows the SDSS luminosity function (Blanton et al. 2003; Gavazzi et al. 2007), with the assumption that  $M_{\text{star}}/L = 4.4$ ; the upper dotted line represents the assumption that  $M_{\text{star}}/L \propto L^{0.25}$ .

lar mass function is insensitive to this parameter: doubling  $\eta$  causes very little change to the mass function above  $2 \times 10^{10} h^{-1} M_{\odot}$ .

The value of  $R_A$  is set to match the observed size distribution of SDSS galaxies. Shen et al. (2003), using the stellar masses of Kauffmann et al. (2003), find that the Sérsic half-light radius of early-type galaxies varies with stellar mass as  $M^{0.56}$ . When using the above procedure on the lowest redshift planes, we find that the

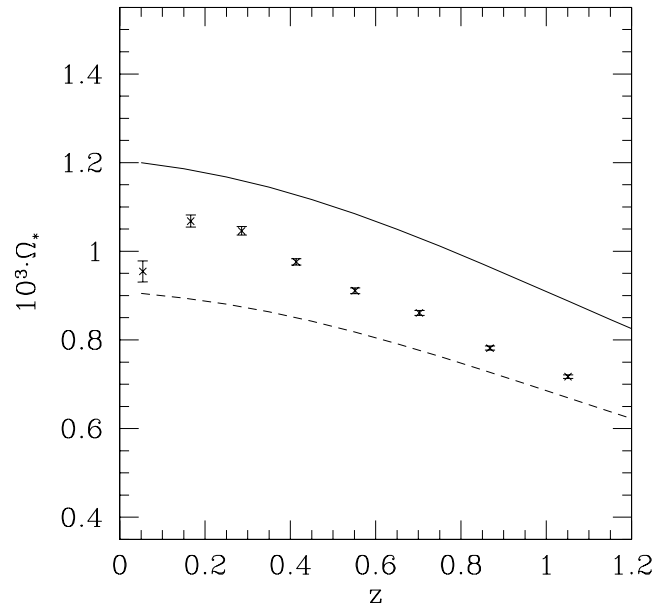


FIG. 3.—Total rearranged “stellar” mass as a function of redshift (determined by applying the baryon redistribution recipe described in § 2.1). The solid line represents an empirically based estimate of the total mass in elliptical galaxies from Nagamine et al. (2006); the dashed line is limited to systems with  $V_c > 215 \text{ km s}^{-1}$ , which would produce a splitting angle of  $>3''$ .

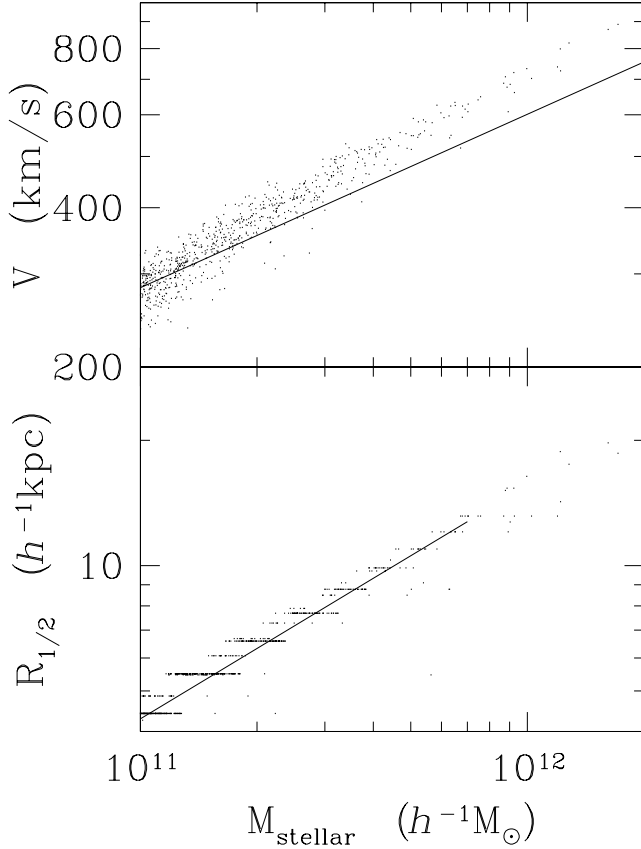


FIG. 4.—*Top*: Circular velocity  $V$  at  $R_A$  as a function of stellar mass  $M_{\text{stellar}}$ , for halos identified in the  $z = 0.05$  and  $0.17$  lens planes. The line indicates the circular velocity measured at  $2.2$  disk lengths by Pizagno et al. (2005). *Bottom*: Half-mass radius  $R_{1/2}$  of the redistributed mass as a function of stellar mass  $M_{\text{stellar}}$ . The line indicates the Sérsic half-light radius of early-type galaxies from SDSS; see Shen et al. (2003).

cooling radius  $R_c$  varies with the mass removed as  $R_c \propto M_{\text{stellar}}^{0.20}$ . Thus, by setting

$$R_A = R_c \left( \frac{M_{\text{stellar}}}{2.4 \times 10^{13} h^{-1} M_{\odot}} \right)^{0.36}, \quad (8)$$

the half-mass radius of the added mass matches the half-light versus radius relation of Shen et al. (2003) for early-type galaxies very well; this is shown at low redshifts in the bottom panel of Figure 4. If this choice of  $R_A$  would result in mass being added to a pixel that is below the background density (i.e.,  $\sigma_i < \sigma_{\text{bg}}$ ), we instead reduce  $R_A$  to the level where this will not occur; it is quite rare that this adjustment is invoked.

The value of  $R_A$  also sets the isothermal circular velocity,  $V_c = 2(GA)^{1/2}$ . The top panel of Figure 4 displays the circular velocity measured at  $R_A$  as a function of stellar mass. These velocities agree reasonably well with the relation between stellar mass and rotation velocity at  $2.2$  disk lengths measured by Pizagno et al. (2005), who find that  $V_{2.2}$  increases with stellar mass roughly as  $M_{\text{stellar}}^{1/3}$ . At higher stellar masses, our circular velocity is about 10% higher than the measured value of  $V_{2.2}$ . A lower limit on the isothermal circular velocity is imposed: for  $V_c < 125 \text{ km s}^{-1}$ , the halo is simply returned to its original density profile. This excludes small overdensities that may be due to minor fluctuations or projection effects. This velocity cut also puts a lower limit on the splitting angles affected by this procedure, which is of order  $1''$ .

To summarize this section, the simple procedure described here reproduces the stellar mass function of large galaxies as a function of redshift, with the appropriate sizes and circular velocities. In § 3 we investigate what effects these galaxies with rearranged matter distribution have quantitatively on the lensing frequency.

## 2.2. Mass Planes, Ray Shooting, and Identification of Arcs

The methods used to create the mass distribution in the lensing planes and to carry out the ray tracing are described in detail in Wambsganss et al. (2004). Here we briefly summarize the procedure and give the numerical values of our parameters. Essentially, light rays are followed backward from the observer through a series of lens planes, approximating a three-dimensional matter distribution; the lens planes are obtained from  $N$ -body simulations (Bode & Ostriker 2003). The parameters of the underlying cosmological model are  $\Omega_M = 0.3$ ,  $\Omega_{\Lambda} = 0.7$ ,  $H_0 = 70 \text{ km s}^{-1} \text{ Mpc}^{-1}$ ,  $\sigma_8 = 0.95$ , and  $n_s = 1$ . The  $N$ -body simulation was performed in a box with a comoving side length of  $L = 320 h^{-1} \text{ Mpc}$ . We used  $N = 1024^3$  particles, so the individual particle mass is  $m_p = 2.54 \times 10^9 h^{-1} M_{\odot}$ . The cubic spline softening length for all particles was set to  $\epsilon = 3.2 h^{-1} \text{ kpc}$ . The output was stored at 19 redshift values out to  $z \approx 6.4$ , such that the centers of the saved boxes matched comoving distances of  $(160 + 320n) h^{-1} \text{ Mpc}$ , where  $n = 0, \dots, 18$ .

For 243 lines of sight traversing the box, two lens planes were produced by bisecting along the line of sight and projecting the mass in each  $160 h^{-1} \text{ Mpc}$  long volume onto a plane. In the lowest redshift box the lensing planes are  $1.9 h^{-1} \text{ Mpc}$  on a side, and the pixel size is  $l = 2.3 h^{-1} \text{ kpc}$ . With increasing lens redshift, we keep the number of pixels constant but increase the physical size of the planes, such that the pixel opening angle remains constant.

Light rays are then propagated backward through these lens planes, beginning with a regular grid at the lowest redshift lens plane (i.e., the image plane) and working to higher redshift by considering the proper deflection in each lens plane. For each source redshift, the coordinates of the rays in the image plane and in the source plane are stored. For analyzing the imaging properties, we impose a regular grid of sources in the source plane and identify for each source position the image multiplicity (by far most of them are single images; some are triples; we also identify quintuples, septuples, etc.), and then for each image the corresponding image position and image magnification.

In the literature, different authors use different definitions for what an “arc” is. As stated in Wambsganss et al. (2004), we demand as a minimum requirement that an arc be part of a multiple image system *and* have a certain minimum magnification (we looked at different values between  $\mu > 5$  and  $\mu > 25$  as limits; the curves in Fig. 6 represent the magnification  $\mu > 5$  threshold; for all curves, at least 90% of the cases have magnification higher than  $\mu > 10$ ). Strongly lensed images are almost always highly distorted in the tangential direction. Williams & Lewis (1998) investigated this quantitatively and found that less than 16% of highly magnified images are elongated in both directions and hence would not be counted as arcs. They find that this fraction decreases strongly with increasing magnification threshold (and with increasing source redshift). The fraction of highly magnified undistorted images decreases even more with the additional requirement that the strongly magnified image be part of a *multiply imaged system*. The magnification of such images is in general close to the length-to-width ratio. We double-checked this assumption in a number of individual cases and found agreement

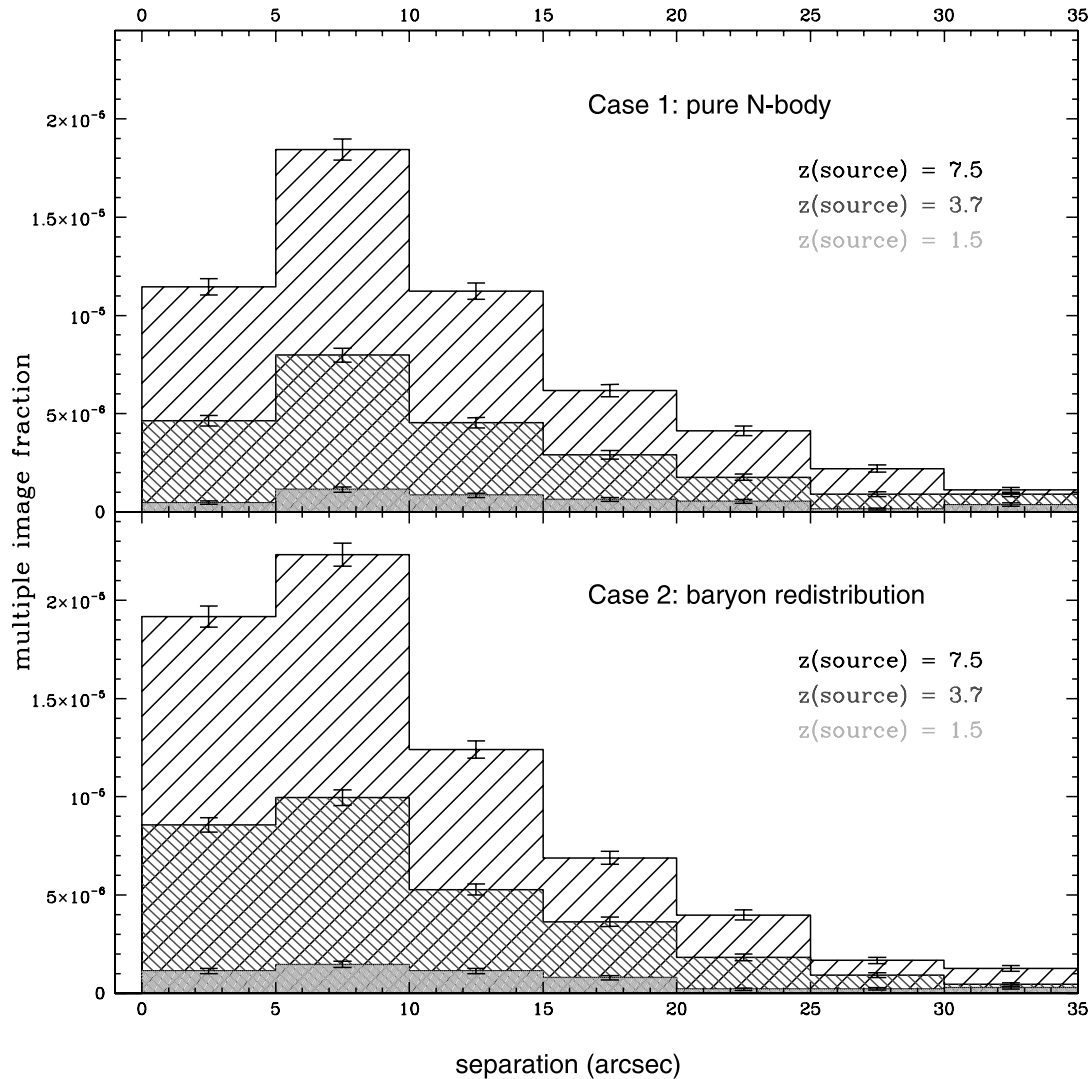


FIG. 5.—Frequency of multiple images as a function of separation (binned with  $5''$  width). The number of multiple images clearly increases with decreasing splitting angle; the drop in the smallest separation bin is due to the fact that our data are highly incomplete for splitting angles below  $3''$ . The  $N$ -body case is shown in the top panel, and the scenario with baryon redistribution is shown in the bottom panel. The histograms reflect three different source redshifts:  $z_s = 7.5$  (hatched histogram),  $z_s = 3.7$  (cross-hatched histogram), and  $z_s = 1.5$  (filled histogram). In the baryon redistribution scenario (bottom), we find more multiple images (on average about 25%); this is most pronounced in the small-separation regime. [See the electronic edition of the Journal for a color version of this figure.]

at well above the 90% level. A detailed discussion of this issue can be found in Wambsganss et al. (2004).

For the multiply imaged sources, we order the images by magnification and determine the distances between the images, whereby the “image separation” is defined as the angular distance between the brightest and the third brightest image (cf. Wambsganss et al. 2004, 2005).

### 3. RAY-SHOOTING RESULTS AND COMPARISON WITH OBSERVATIONS

#### 3.1. Ray Shooting

We performed two complete sets of ray-shooting simulations as detailed in § 2.2, once with the original pure  $N$ -body matter screens and once with the new recipe of rearranged matter, creating 100 independent realizations for each of the two sets. This procedure allowed us to study the effect both statistically and on individual lines of sight (the latter turned out to be essential for a complete understanding of the results, as described below). Three source redshifts are considered:  $z_s = 1.5$ ,  $3.7$ , and  $7.5$ .

With the rearrangement, the number of multiple images increased for all source redshifts, particularly for angular separations of up to  $15''$ . This is shown in Figure 5, where the multiple-image cases are binned according to the image splitting, with bin widths of  $5''$  (note that our data are highly incomplete in the first bin, because we do not properly resolve image splittings smaller than about  $3''$ ). The level of increase can be read off of the integrated distributions in Figure 6, where the dashed lines show the integrated frequency of multiple images as a function of separation for the pure  $N$ -body case and the solid lines show the scenario with baryon rearrangement. Note that for all these cases there is a second requirement imposed, namely, that at least one of the multiple images must be magnified by more than a factor of 5. Qualitatively, it is obvious that including the baryon redistribution produces more multiple images. The relative amount by which the rearranged case is higher than the pure  $N$ -body case is almost independent of source redshift: the fraction is about 25% for the redshift range  $z_s = 1.5$ – $7.5$  (it varies between 22% and 28%). Beyond the total lensing frequencies, it is interesting to study the *differential* effect: it is for relatively small separations

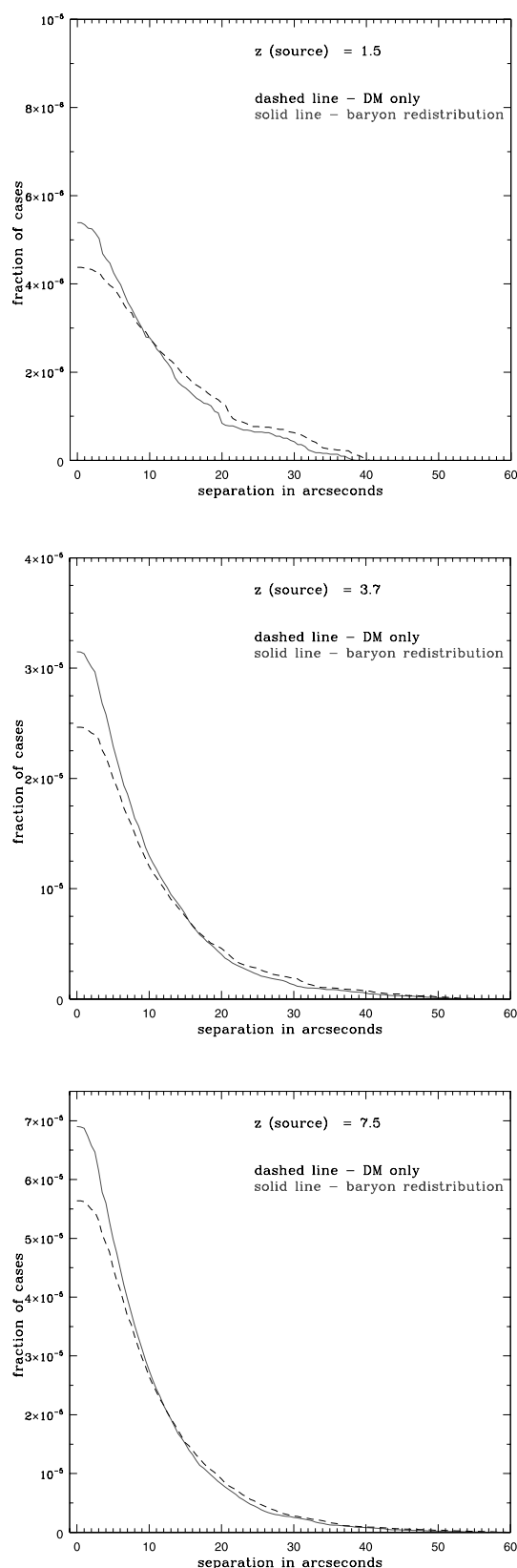


FIG. 6.—Integrated probability distribution of arcs (i.e., multiple image systems with at least one image above a magnification of  $\mu_i \geq 5$ ; for all curves, more than 90% of the cases have an image with a magnification of  $\mu_i \geq 10$ ) as a function of separation for a dark matter-only simulation (*dashed line*) and with baryon redistribution as described in the text (*solid line*). *Top*, Source redshift  $z_s = 1.5$ ; *middle*,  $z_s = 3.7$ ; *bottom*,  $z_s = 7.5$ . [See the electronic edition of the *Journal* for a color version of this figure.]

( $\leq 10''$ ) in particular that the baryon redistribution case leads to more multiple images: about a 70% increase in the lowest bin, and a 30% increase in the  $5''$ – $10''$  bin. This increase is easy to understand: the baryon redistribution steepens the innermost parts of the density profiles of halos and hence can bring DM halos that are originally just below the critical density for lensing above this value, thus producing multiple images. The excess decreases with increasing separation, such that at a splitting of  $\sim 12''$ – $15''$  the two cases result in the same frequencies for multiple images.

At still larger separations, the baryon redistribution case apparently produces slightly fewer cases (at the level of a few percent). This behavior is not quite obvious; in fact, it is rather counterintuitive. To first order, the expected increases are independent of the total mass of the halos; i.e., even massive cluster-type halos can get boosted above the critical surface mass density in the center and produce arcs after the redistribution has been applied. And if a fraction of the total mass becomes more concentrated, the total mass inside an image pair should be the same or larger. However, apparently more intermediate-mass halos fulfill this criterion than do halos at the highest mass end.

The explanation for this apparent discrepancy—that the proper treatment of baryon cooling increases preferentially small- and intermediate-separation image splittings—is that this effect is just an artifact of our definition of image separation. As described above, we define the separation of a multiple-image system as the angular distance between the brightest and the third brightest image. Our method always identifies the “odd” image in triples and quintuples, although in practice most would be identified as double and quadruple images, because the odd images in most observational situations are demagnified and not detectable (hence, we refer subsequently to those cases as “doubles” and “quadruples”). A detailed look at the distribution of multiple images shows that a side effect of the redistribution of baryons is that the number of quadruple images increases more strongly than does the number of doubles (see Fig. 7). We are able to verify this by comparing individual lines of sight, with and without the matter rearrangement. When we compare one-to-one a situation that produces a double image in the DM-only scenario and a quadruple image in the baryon redistribution case, the additional image pair occasionally is brighter than the faint “odd” image, and it happens that this pair is close to the brightest image of the multiplet, resulting in a smaller measured image separation than in the pure  $N$ -body case: i.e., this multiple image in the baryon redistribution simulation adds to the multiples in a smaller separation image bin than it did in the pure  $N$ -body case. This leads to the apparent small deficit of large-separation cases in the redistributed baryon case.

### 3.2. Comparison with Observations and with Other Simulations

Over the last decade, various papers have investigated the observational occurrence of giant arcs statistically: e.g., Luppino et al. (1999), Gladders et al. (2003), Zaritsky & Gonzalez (2003), and Sand et al. (2005). The frequency of arcs reported in these studies varies from one giant arc per  $45 \text{ deg}^2$  to about one arc per  $10 \text{ deg}^2$ ; the large spread may be explained partly by the slightly different definitions and limiting magnitudes and may be related to the relatively small number of cases per study. Overall, just about 50 arc systems, found in various surveys with diverse selection criteria, had been used for these statistical analyses. In general terms, the results between observations and predictions for a concordance cosmological model agree with each other (cf. the more detailed discussion in Wambsganss et al. 2004).

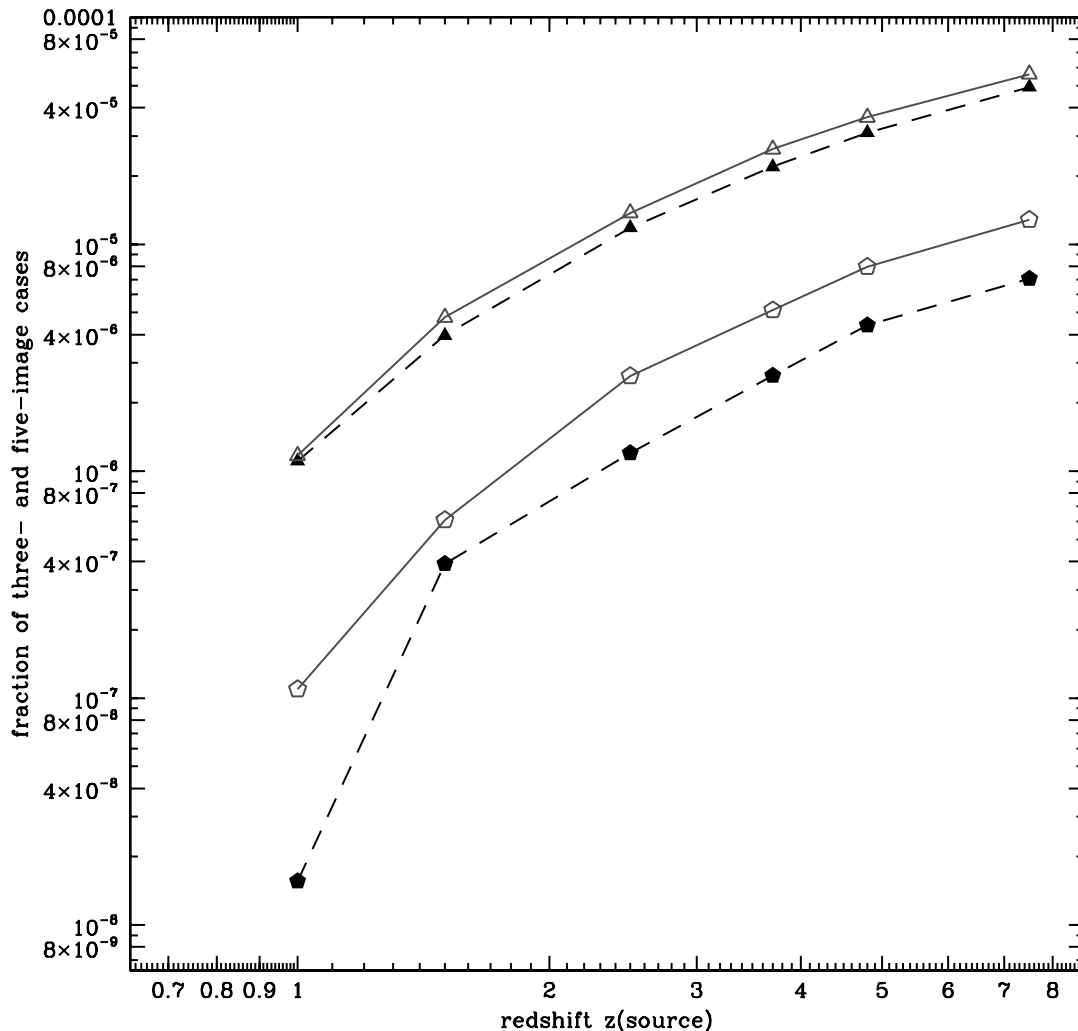


FIG. 7.—Image multiplicity as a function of source redshift for triple images (*triangles*) and quintuple images (*pentagons*). The pure  $N$ -body case is shown with filled symbols and dashed lines; for the baryon rearrangement case we used open symbols and solid lines. [See the electronic edition of the *Journal* for a color version of this figure.]

Two recent studies based on SDSS data present quite interesting results, partly contradicting each other. On the one hand, Estrada et al. (2007) report no arcs found in a systematic investigation of 825 SDSS clusters (other than one serendipitous discovery). On the other hand, Hennawi et al. (2008) presented preliminary results from a new survey for giant arcs that may as much as double the number of known arcs (about 30 new systems already reported). This study is very promising, not just because of the large number of new arc systems to be expected, but, at least as importantly, also because it will find them by well-defined selection criteria.

Until the quantitative results of that study are published, we can compare our results here “differentially” to those in Wambsganss et al. (2004). There it was concluded that the simulated pure  $N$ -body-based arc frequencies are consistent with the observations, if we allow the source redshifts to extend well beyond  $z \geq 1$  (as the distribution of observed arcs does as well). Since the incidence of arcs steeply increases with source redshift, as was found in Wambsganss et al. (2004), the apparent order-of-magnitude discrepancy between the number of predicted and detected arcs (cf. Bartelmann et al. 1998) essentially disappeared.

Our new results presented in this paper are based on a more realistic modeling of the baryons in the centers of halos (compared to the pure  $N$ -body treatment in Wambsganss et al. 2004).

This treatment increases the probability of arcs by about 25%. Qualitatively, this works in the same direction as the results of Meneghetti et al. (2003): they found that adding a cD galaxy to the center of a cluster moderately increases the probability for strong lensing. Our findings are also qualitatively consistent with the study of Puchwein et al. (2005; although quantitatively our results are lower than theirs): they investigated various effects of gas physics on strong lensing by studying individual clusters and found that cooling steepens the mass density profiles in the halo cores. They concluded that, as a consequence, this cooling effect can increase the strong-lensing efficiency considerably.

In principle, we can also compare our results with large-separation multiple quasars. However, on the observational side, the number of those is still relatively small, and no statistical analysis of the results has yet been made. The few examples discovered recently, such as the  $15''$  separation quasar SDSS J1004+4112 (Inada et al. 2003; Fohlmeister et al. 2007), give rise to some optimism that such analyses will be possible soon.

The result presented here—that by including the baryon rearrangement, the predicted number of arcs (i.e., multiple-image systems with at least one image above a certain magnification threshold) increases by about 25%—puts the predicted arc frequency a bit on the high side compared with the observations, but there is still considerable uncertainty on both the observational

(e.g., absolute numbers, selection criteria) and the theoretical sides (e.g., parameters of underlying cosmological model, exact definition of “arc”). In particular, the model used here has a high normalization for the amplitude of fluctuations as compared to the recent results from *WMAP*; a lower normalization would significantly reduce the lensing frequency (Li et al. 2007).

#### 4. SUMMARY AND CONCLUSION

This paper quantitatively investigates the effects on lensing of baryon redistribution in originally pure dark matter  $N$ -body simulations. We describe a heuristic recipe for rearranging the baryons in dense dark matter halos that is consistent with observational data for massive galaxies, present a number of tests of this prescription, and then apply it to a cosmological simulation used for multiple lens plane ray shooting. We compare the frequency of multiple images, the image separation, and the image multiplicity between the original  $N$ -body matter distribution and the redistributed version.

We find that on average, the case that takes into account the redistribution of baryons produces 25% more multiple images/arcs; this is almost independent of the source redshift in the range  $z_s = 1.5$ – $7.5$ . For splittings between  $5''$  and  $10''$ , the number of multiple images increases by roughly 30%, and it increases by 70% for smaller separations ( $<5''$ ). But this last result must be treated with caution, since our data are resolution-limited for splittings of  $\lesssim 3''$ . Most of the new multiple-image systems occur for angular scales of  $\leq 10''$ . We also find that the number of quadruple

images increases more than does the number of double images. This produces an apparent slight reduction of larger separation cases, which is in fact only an artifact of the way that we define image separation; namely, as the distance between the brightest and the third brightest images.

Since arc statistics are such a good tool for distinguishing between models with different cosmological parameters, we would like to emphasize once again the need for both very good observational studies and for more explorations of the important parameters in the simulations.

This work was supported by the European Community’s Sixth Framework Marie Curie Research Training Network Programme, contract MRTN-CT-2004-505183 “ANGLES.” This research was also facilitated through an allocation of advanced computing resources from the National Center for Supercomputing Applications (under grant MCA04N002) and the Pittsburgh Supercomputing Center. In addition, computational facilities at Princeton supported by NSF grant AST 02-16105 were used, as well as high-performance computational facilities supported by Princeton University under the auspices of the Princeton Institute for Computational Science and Engineering (PICSciE) and the Office of Information Technology (OIT). We thank an unknown referee for many good suggestions that helped to clarify and improve the manuscript significantly.

#### REFERENCES

- Bahcall, N. A., & Bode, P. 2003, *ApJ*, 588, L1  
 Bahcall, N. A., & Cen, R. 1993, *ApJ*, 407, L49  
 Bartelmann, M., Huss, A., Colberg, J. M., Jenkins, A., & Pearce, F. R. 1998, *A&A*, 330, 1  
 Blanton, M. R., et al. 2003, *ApJ*, 592, 819  
 Bode, P., & Ostriker, J. P. 2003, *ApJS*, 145, 1  
 Cox, A. N., ed. 2000, *Allen’s Astrophysical Quantities* (4th ed.; New York: AIP)  
 Dalal, N., Holder, G., & Hennawi, J. F. 2004, *ApJ*, 609, 50  
 Eke, V. R., Cole, S., & Frenk, C. S. 1996, *MNRAS*, 282, 263  
 Estrada, J., et al. 2007, *ApJ*, 660, 1176  
 Evrard, A. E., et al. 2008, *ApJ*, 672, 122  
 Fohlmeister, J., et al. 2007, *ApJ*, 662, 62  
 Gavazzi, R., Treu, T., Rhodes, J. D., Koopmans, L. V. E., Bolton, A. S., Burles, S., Massey, R. J., & Moustakas, L. A. 2007, *ApJ*, 667, 176  
 Gladders, M., Hoekstra, H., Yee, H. K. C., Hall, P. B., & Barrientos, L. F. 2003, *ApJ*, 593, 48  
 Hennawi, J. F., Dalal, N., & Bode, P. 2007a, *ApJ*, 654, 93  
 Hennawi, J. F., Dalal, N., Bode, P., & Ostriker, J. P. 2007b, *ApJ*, 654, 714  
 Hennawi, J. F., et al. 2008, *AJ*, 135, 664  
 Henry, J. P., & Arnaud, K. A. 1991, *ApJ*, 372, 410  
 Hilbert, S., White, S. D. M., Hartlap, J., & Schneider, P. 2007, *MNRAS*, 382, 121  
 Ho, S., & White, M. 2005, *Astrophys. J.*, 24, 257  
 Horesh, A., Ofek, E. O., Maoz, D., Bartelmann, M., Meneghetti, M., & Rix, H.-W. 2005, *ApJ*, 633, 768  
 Inada, N., et al. 2003, *Nature*, 426, 810  
 ———. 2005, *PASJ*, 57, L7  
 ———. 2006, *ApJ*, 653, L97  
 Jing, Y. P., Zhang, P., Lin, W. P., Gao, L., & Springel, V. 2006, *ApJ*, 640, L119  
 Kauffmann, G., et al. 2003, *MNRAS*, 341, 33  
 Li, G.-L., Mao, S., Jing, Y. P., Bartelmann, M., Kang, X., & Meneghetti, M. 2005, *ApJ*, 635, 795  
 Li, G. L., Mao, S., Jing, Y. P., Lin, W. P., & Oguri, M. 2007, *MNRAS*, 378, 469  
 Li, L.-X., & Ostriker, J. P. 2002, *ApJ*, 566, 652  
 ———. 2003, *ApJ*, 595, 603  
 Lin, W. P., Jing, Y. P., Mao, S., Gao, L., & McCarthy, I. G. 2006, *ApJ*, 651, 636  
 Luppino, G. A., Gioia, I. M., Hammer, F., Le Fèvre, O., & Annis, J. A. 1999, *A&AS*, 136, 117  
 Meneghetti, M., Bartelmann, M., & Moscardini, L. 2003, *MNRAS*, 346, 67  
 Nagamine, K., Ostriker, J. P., Fukugita, M., & Cen, R. 2006, *ApJ*, 653, 881  
 Oguri, M., & Keeton, C. R. 2004, *ApJ*, 610, 663  
 Oguri, M., et al. 2004, *ApJ*, 605, 78  
 Oukbir, J., & Blanchard, A. 1992, *A&A*, 262, L21  
 Peng, E. W., Ford, H., & Freeman, K. 2004, *ApJ*, 602, 685  
 Pizagno, J., et al. 2005, *ApJ*, 633, 844  
 Puchwein, E., Bartelmann, M., Dolag, K., & Meneghetti, M. 2005, *A&A*, 442, 405  
 Rozo, E., Nagai, D., Keeton, C., & Kravtsov, A. 2006, *ApJ*, submitted (astro-ph/0609621)  
 Sand, D. J., Treu, T., Ellis, R. S., & Smith, G. P. 2005, *ApJ*, 627, 32  
 Sharon, K., et al. 2005, *ApJ*, 629, L73  
 Shen, S., Mo, H. J., White, S. D. M., Blanton, M. R., Kauffmann, G., Voges, W., Brinkmann, J., & Csabai, I. 2003, *MNRAS*, 343, 978  
 Spergel, D. N., et al. 2007, *ApJS*, 170, 377  
 Turner, E. L. 1990, *ApJ*, 365, L43  
 Vale, A., & Ostriker, J. P. 2006, *MNRAS*, 371, 1173  
 Viana, P. P., & Liddle, A. R. 1996, *MNRAS*, 281, 323  
 Wambsganss, J., Bode, P., & Ostriker, J. P. 2004, *ApJ*, 606, L93  
 ———. 2005, *ApJ*, 635, L1  
 Wambsganss, J., Cen, R., & Ostriker, J. P. 1998, *ApJ*, 494, 29  
 Wambsganss, J., Cen, R., Ostriker, J. P., & Turner, E. L. 1995, *Science*, 268, 274  
 Wambsganss, J., Cen, R., Xu, G., & Ostriker, J. P. 1997, *ApJ*, 475, L81  
 White, S. D. M., Efstathiou, G., & Frenk, C. S. 1993, *MNRAS*, 262, 1023  
 Williams, L. L. R., & Lewis, G. 1998, *MNRAS*, 294, 299  
 Zaritsky, D., & Gonzalez, A. H. 2003, *ApJ*, 584, 691

*Note added in proof.*—After acceptance of our paper, a preprint by S. Hilbert et al. (2007, *MNRAS*, submitted [arXiv:0712.1593]) came to our attention that treats a question very similar to the one we addressed here. Qualitatively their results look very similar to ours; the quantitative differences are probably a consequence of the different normalizations and effective resolutions of the two approaches.